The Astrophysical Journal, 945:52 (14pp), 2023 March 1 https://doi.org/10.3847/1538-4357/acb496

X-Ray Polarimetry Reveals the Magnetic-field Topology on Sub-parsec Scales in Tycho's Supernova Remnant

Riccardo Ferrazzoli[1], Patrick Slane[2], Dmitry Prokhorov[3], Ping Zhou[4], Jacco Vink[3], Niccolò Bucciantini[5,6,7], Enrico Costa[1], Niccolò Di Lalla[8], Alessandro Di Marco[1], Paolo Soffitta[1], Martin C. Weisskopf[9], Kazunori Asakura[10], Luca Baldini[11,12], Jeremy Heyl[13], Philip E. Kaaret[9], Frédéric Marin[14], Tsunefumi Mizuno[15], C.-Y. Ng[16], Melissa Pesce-Rollins[11], Stefano Silvestri[11], Carmelo Sgrò[11], Douglas A. Swartz[17], Toru Tamagawa[18], Yi-Jung Yang[16], Iván Agudo[19], Lucio A. Antonelli[20,21], Matteo Bachetti[22], Wayne H. Baumgartner[9], Ronaldo Bellazzini[11], Stefano Bianchi[23], Stephen D. Bongiorno[9], Raffaella Bonino[24,25], Alessandro Brez[11], Fiamma Capitanio[1], Simone Castellano[11], Elisabetta Cavazzuti[26], Chien-Ting Chen[17], Stefano Ciprini[21,27], Alessandra De Rosa[1], Ettore Del Monte[1], Laura Di Gesu[26], Immacolata Donnarumma[26], Victor Doroshenko[28], Michal Dovčiak[29], Steven R. Ehlert[9], Teruaki Enoto[18], Yuri Evangelista[1], Sergio Fabiani[1], Javier A. Garcia[30], Shuichi Gunji[31], Kiyoshi Hayashida[32,53], Wataru Iwakiri[33], Svetlana G. Jorstad[34,35], Fabian Kislat[36], Vladimir Karas[29], Takao Kitaguchi[18], Jeffery J. Kolodziejczak[9], Henric Krawczynski[37], Fabio La Monaca[1], Luca Latronico[24], Ioannis Liodakis[38], Simone Maldera[24], Alberto Manfreda[11], Andrea Marinucci[26], Alan P. Marscher[34], Herman L. Marshall[25,39], Giorgio Matt[23], Ikuyuki Mitsuishi[40], Fabio Muleri[1], Michela Negro[41,42,43], Stephen L. O'Dell[9], Nicola Omodei[8], Chiara Oppedisano[24], Alessandro Papitto[20], George G. Pavlov[44], Abel L. Peirson[8], Matteo Perri[20,21], Pierre-Olivier Petrucci[45], Maura Pilia[22], Andrea Possenti[22], Juri Poutanen[46], Simonetta Puccetti[21], Brian D. Ramsey[9], John Rankin[1], Ajay Ratheesh[1], Oliver Roberts[17], Roger W. Romani[8], Gloria Spandre[11], Fabrizio Tavecchio[47], Roberto Taverna[48], Yuzuru Tawara[40], Allyn F. Tennant[9], Nicholas E. Thomas[9], Francesco Tombesi[27,49,50], Alessio Trois[22], Sergey S. Tsygankov[46], Roberto Turolla[48,51], Kinwah Wu[51], Fei Xie[1,52], and Silvia Zane[51]

[1] INAF Istituto di Astrofisica e Planetologia Spaziali, Via del Fosso del Cavaliere 100, I-00133 Roma, Italy; riccardo.ferrazzoli@inaf.it
[2] Center for Astrophysics | Harvard & Smithsonian, 60 Garden Street, Cambridge, MA 02138, USA
[3] Anton Pannekoek Institute for Astronomy & GRAPPA, University of Amsterdam, Science Park 904, 1098 XH Amsterdam, The Netherlands
[4] School of Astronomy and Space Science, Nanjing University, Nanjing 210023, People's Republic of China
[5] INAF Osservatorio Astrofisico di Arcetri, Largo Enrico Fermi 5, I-50125 Firenze, Italy
[6] Dipartimento di Fisica e Astronomia, Università degli Studi di Firenze, Via Sansone 1, I-50019 Sesto Fiorentino (FI), Italy
[7] Istituto Nazionale di Fisica Nucleare, Sezione di Firenze, Via Sansone 1, I-50019 Sesto Fiorentino (FI), Italy
[8] Department of Physics and Kavli Institute for Particle Astrophysics and Cosmology, Stanford University, Stanford, CA 94305, USA
[9] NASA Marshall Space Flight Center, Huntsville, AL 35812, USA
[10] Osaka University, Graduate School of Science, Osaka, Japan
[11] Istituto Nazionale di Fisica Nucleare, Sezione di Pisa, Largo B. Pontecorvo 3, I-56127 Pisa, Italy
[12] Dipartimento di Fisica, Università di Pisa, Largo B. Pontecorvo 3, I-56127 Pisa, Italy
[13] University of British Columbia, Vancouver, BC V6T 1Z4, Canada
[14] Université de Strasbourg, CNRS, Observatoire Astronomique de Strasbourg, UMR 7550, F-67000 Strasbourg, France
[15] Hiroshima Astrophysical Science Center, Hiroshima University, 1-3-1 Kagamiyama, Higashi-Hiroshima, Hiroshima 739-8526, Japan
[16] Department of Physics, The University of Hong Kong, Pokfulam, Hong Kong
[17] Science and Technology Institute, Universities Space Research Association, Huntsville, AL 35805, USA
[18] RIKEN Cluster for Pioneering Research, 2-1 Hirosawa, Wako, Saitama 351-0198, Japan
[19] Instituto de Astrofísica de Andalucía, CSIC, Glorieta de la Astronomía s/n, E-18008 Granada, Spain
[20] INAF Osservatorio Astronomico di Roma, Via Frascati 33, I-00078 Monte Porzio Catone (RM), Italy
[21] Space Science Data Center, Agenzia Spaziale Italiana, Via del Politecnico snc, I-00133 Roma, Italy
[22] INAF Osservatorio Astronomico di Cagliari, Via della Scienza 5, I-09047 Selargius (CA), Italy
[23] Dipartimento di Matematica e Fisica, Università degli Studi Roma Tre, Via della Vasca Navale 84, I-00146 Roma, Italy
[24] Istituto Nazionale di Fisica Nucleare, Sezione di Torino, Via Pietro Giuria 1, I-10125 Torino, Italy
[25] Dipartimento di Fisica, Università degli Studi di Torino, Via Pietro Giuria 1, I-10125 Torino, Italy
[26] ASI—Agenzia Spaziale Italiana, Via del Politecnico snc, I-00133 Roma, Italy
[27] Istituto Nazionale di Fisica Nucleare, Sezione di Roma "Tor Vergata," Via della Ricerca Scientifica 1, I-00133 Roma, Italy
[28] Institut für Astronomie und Astrophysik, Universität Tübingen, Sand 1, D-72076 Tübingen, Germany
[29] Astronomical Institute of the Czech Academy of Sciences, Boční II 1401/1, 14100 Praha 4, Czech Republic
[30] California Institute of Technology, Pasadena, CA 91125, USA
[31] Yamagata University, 1-4-12 Kojirakawa-machi, Yamagata-shi 990-8560, Japan
[32] Osaka University, 1-1 Yamadaoka, Suita, Osaka 565-0871, Japan
[33] Department of Physics, Faculty of Science and Engineering, Chuo University, 1-13-27 Kasuga, Bunkyo-ku, Tokyo 112-8551, Japan
[34] Institute for Astrophysical Research, Boston University, 725 Commonwealth Avenue, Boston, MA 02215, USA
[35] Department of Astrophysics, St. Petersburg State University, Universitetsky pr. 28, Petrodvoretz, 198504 St. Petersburg, Russia
[36] Department of Physics and Astronomy and Space Science Center, University of New Hampshire, Durham, NH 03824, USA
[37] Physics Department and McDonnell Center for the Space Sciences, Washington University in St. Louis, St. Louis, MO 63130, USA
[38] Finnish Centre for Astronomy with ESO, FI-20014 University of Turku, Finland
[39] MIT Kavli Institute for Astrophysics and Space Research, Massachusetts Institute of Technology, 77 Massachusetts Avenue, Cambridge, MA 02139, USA
[40] Graduate School of Science, Division of Particle and Astrophysical Science, Nagoya University, Furo-cho, Chikusa-ku, Nagoya, Aichi 464-8602, Japan
[41] University of Maryland, Baltimore County, Baltimore, MD 21250, USA
[42] NASA Goddard Space Flight Center, Greenbelt, MD 20771, USA
[43] Center for Research and Exploration in Space Science and Technology, NASA/GSFC, Greenbelt, MD 20771, USA
[44] Department of Astronomy and Astrophysics, Pennsylvania State University, University Park, PA 16802, USA
[45] Université Grenoble Alpes, CNRS, IPAG, F-38000 Grenoble, France
[46] Department of Physics and Astronomy, FI-20014 University of Turku, Finland

[47] INAF Osservatorio Astronomico di Brera, Via E. Bianchi 46, I-23807 Merate (LC), Italy
[48] Dipartimento di Fisica e Astronomia, Università degli Studi di Padova, Via Marzolo 8, I-35131 Padova, Italy
[49] Dipartimento di Fisica, Università degli Studi di Roma "Tor Vergata," Via della Ricerca Scientifica 1, I-00133 Roma, Italy
[50] Department of Astronomy, University of Maryland, College Park, MD 20742, USA
[51] Mullard Space Science Laboratory, University College London, Holmbury St Mary, Dorking, Surrey RH5 6NT, UK
[52] Guangxi Key Laboratory for Relativistic Astrophysics, School of Physical Science and Technology, Guangxi University, Nanning 530004, People's Republic of China
Received 2022 December 22; revised 2023 January 17; accepted 2023 January 17; published 2023 March 7

Abstract

Supernova remnants are commonly considered to produce most of the Galactic cosmic rays via diffusive shock acceleration. However, many questions regarding the physical conditions at shock fronts, such as the magnetic-field morphology close to the particle acceleration sites, remain open. Here we report the detection of a localized polarization signal from some synchrotron X-ray emitting regions of Tycho's supernova remnant made by the Imaging X-ray Polarimetry Explorer. The derived degree of polarization of the X-ray synchrotron emission is $9\% \pm 2\%$ averaged over the whole remnant, and $12\% \pm 2\%$ at the rim, higher than the value of polarization of 7%–8% observed in the radio band. In the west region, the degree of polarization is $23\% \pm 4\%$. The degree of X-ray polarization in Tycho is higher than for Cassiopeia A, suggesting a more ordered magnetic field or a larger maximum turbulence scale. The measured tangential direction of polarization corresponds to the radial magnetic field, and is consistent with that observed in the radio band. These results are compatible with the expectation of turbulence produced by an anisotropic cascade of a radial magnetic field near the shock, where we derive a magnetic-field amplification factor of 3.4 ± 0.3. The fact that this value is significantly smaller than those expected from acceleration models is indicative of highly anisotropic magnetic-field turbulence, or that the emitting electrons either favor regions of lower turbulence, or accumulate close to where the orientation of the magnetic field is preferentially radially oriented due to hydrodynamical instabilities.

Unified Astronomy Thesaurus concepts: Supernova remnants (1667); Polarimetry (1278); X-ray astronomy (1810)

1. Introduction

Supernova remnants (SNRs) are structures bounded by an expanding shock wave driven by material from an exploded star sweeping up the interstellar medium. SNRs accelerate particles to energies of at least hundreds of teraelectronvolts (see, e.g., Ginzburg & Syrovatskii 1964; Amato 2014) and are considered to be a dominant source of the Galactic cosmic rays (CRs) below the knee (∼3 PeV). Diffusive shock acceleration (DSA) is generally accepted as the mechanism of CR acceleration in SNRs (see Malkov & Drury 2001, for a review on the subject). Tycho's SNR (henceforth, Tycho) is the remnant of the historical supernova SN 1572, first recorded in November of 1572 and named after Tycho Brahe (Green & Stephenson 2003). With an age of 450 yr, Tycho is in the ejecta-dominated phase of evolution, slowly transitioning to the Sedov phase (Decourchelle2017). Its magnetic-field strengths and shock velocity are in the range of 50–400 μG (Reynolds et al. 2021) and 3500–4400 km s^{-1} (Williams et al. 2017, 2020), respectively.

Studies of polarization of SNRs in the radio band have been fundamental to proving the synchrotron nature of the observed radiation, and have provided important information on the magnetic-field structures and their connection to particle acceleration (see Dubner & Giacani 2015, for a review). Radio emission from Tycho at 2.8–6 cm is polarized, with typical values of the degree of linear polarization ranging from 0 at the center, to 7%–8% at the outer rim (Kundu & Velusamy 1971; Dickel et al. 1991). The direction of the polarization indicates a large-scale radial magnetic-field structure (Kundu & Velusamy 1971; Strom & Duin 1973; Duin & Strom 1975; Dickel et al. 1991; Reynoso et al. 1997).

Because the teraelectronvolt-energy electrons responsible for the X-ray emission lose energy very fast, they have a very short lifetime compared to the radio-emitting electrons, and are confined to smaller regions, within $\leqslant 10^{17}$ cm—that is, sub-parsec scales—from the acceleration sites. There are two competing ideas for the magnetic-field topology in SNRs on spatial scales accessible in X-rays. On the one hand, shock compression should enhance the magnetic-field component parallel to the shock front, leading to a predominantly tangential magnetic field (Jun & Norman 1996; Bykov et al. 2020); on the other hand, many of the processes suggested for explaining the radial magnetic field in the radio band (e.g., Zirakashvili & Ptuskin 2008; Inoue et al. 2013; West et al. 2017) could be at work already close to the shock (i.e., within linear scales of 10^{17} cm), such as selection effects due to the locus of relativistic electron pileup downstream of the shock, or filamentation due to hydrodynamical instabilities at the contact discontinuity (CD) between shocked ejecta and shocked circumstellar plasma. This dichotomy is also present in observations, with older remnants having tangential magnetic fields and younger remnant radial magnetic fields. Because the CD is not usually close to the shock, Inoue et al. (2013) also discuss the possibility of the presence of Richtmyer–Meshkov instability (Richtmyer 1960).

High-resolution Chandra X-ray observations of Tycho revealed a bright thin synchrotron rim at the shock (Hwang et al. 2002) that matches a similar feature seen in the radio band (Dickel et al. 1991), but also peculiar small-scale (from ∼arcseconds to ∼arcminute) structures in the 4–6 keV band, the so-called *stripes* in the western rim that were first identified by Eriksen et al. (2011). These small-scale structures are variable in time and shape on a scale of a few years (Matsuda et al. 2020; Okuno et al. 2020). The stripes, along with the entire SNR rim, are thought to be CR acceleration sites, and might be the result of fast energy losses of the teraelectronvolt electrons emitting X-rays downstream of the

[53] Deceased.

shock in amplified magnetic fields (Bykov et al. 2011, 2020, and references therein). If that is the case, the synchrotron structures are due to geometric projection of the thin regions where the teraelectronvolt electrons are accelerated.

X-ray polarimetry allows us to determine the orientation (through the direction of the polarization) and turbulence (through the degree of the polarization) of the magnetic field close to the particle acceleration sites (within 10^{17} cm). Measurements of such parameters of polarization are thus fundamental for the study of magnetic-field fluctuations, and for a proper understanding of DSA in young SNRs. For an in-depth discussion of the advantages of polarimetry of SNRs in the X-ray band with respect to the radio band see Vink & Zhou (2018).

The expectation of spatially resolved X-ray polarimetry of SNRs in general, and Tycho in particular, has been discussed by many authors (Bykov et al. 2009, 2011, 2020; Baring 2017; Vink & Zhou 2018). Bykov et al. (2009, 2020) found that highly polarized (∼tens of percent) patchy structures of ∼30″ are potentially observable in high-resolution X-ray images, with the level of polarization depending on the spectrum of magnetic-field fluctuations $\delta B/B$.

The Imaging X-ray Polarimetry Explorer (IXPE; Soffitta et al. 2021; Weisskopf et al. 2022), a NASA mission in partnership with the Italian space agency (ASI), launched in 2021, allows us to perform for the first time spatially resolved X-ray polarimetry with an angular resolution of ∼30″ (half-power diameter) in the 2–8 keV energy band. The first study of the X-ray polarization properties of an SNR was recently reported with the IXPE observation of Cassiopeia A (Cas A; Vink et al. 2022b), which found a radial magnetic field similar to that observed at longer wavelengths, with a low degree of polarization, which implies high levels of turbulence.

Here we report the first spatially resolved X-ray polarimetric observations of Tycho with IXPE, The paper is organized as follows: in Section 2 we describe the IXPE observation and data reduction; in Section 3 we present our results, and finally, we discuss them in Section2 4 and present our conclusions in Section 5. Details of the background removal and treatment of the unpolarized thermal emission of Tycho are presented in Appendix A and B, respectively.

2. Observation and Data Analysis

2.1. Observation Description

As described in detail in Weisskopf et al. (2022) and references therein, the IXPE observatory includes three identical X-ray telescopes, each comprising an X-ray mirror module assembly (NASA provided) and a polarization-sensitive Gas Pixel Detector (GPD; ASI provided), to offer imaging spectropolarimetry in the 2–8 keV band. IXPE data are telemetered to ground stations in Malindi (primary) and in Singapore (secondary), then transmitted to the Mission Operations Center (MOC; at the Laboratory for Atmospheric and Space Physics, University of Colorado), and finally sent to the Science Operations Center (SOC; at the NASA Marshall Space Flight Center). Using a software pipeline jointly developed by ASI and NASA, the SOC processes science and relevant engineering and ancillary data, estimates the direction of photoelectron emission (and hence the polarization), location, and energy of each event after applying corrections for detector temperature, and gain nonuniformity and charging effects of the Gas Electron Multiplier. Spurious polarization is removed using the algorithm of Rankin et al. (2022). Time-and-spatially dependent gain variations of the detectors are corrected employing the onboard calibration sources (Ferrazzoli et al. 2020): during Earth occultations of the source, one Detector Unit (DU) at a time is calibrated with the monochromatic unpolarized sources Cal C or Cal D, respectively, with energy at 5.89 and 1.7 keV. These onboard calibration measurements are used to obtain the best knowledge of the gain of the detectors at the time of the observation, and hence the correct energy of each photon. This allows us to correct the Stokes parameters for the presence of systematic effects and to use the correct value of the modulation factor (see Weisskopf et al. 2022).

The output of this pipeline processing is an event file in FITS format for each of the three IXPE DUs that contains, in addition to the typical information related to spatially resolved X-ray astronomy, the event-by-event Stokes parameters q_k and u_k, with k being the event number, from which the polarization of the radiation can be derived. Since the Stokes parameters are additive for any selection criterion (Kislat et al. 2015), those referring to a given energy band are obtained by simply summing the parameters of all the events in the energy range of interest weighted by the modulation factor.

The data products are archived at the High-Energy Astrophysics Science Archive Research Center (HEASARC; at the NASA Goddard Space Flight Center), for use by the international astrophysics community.

IXPE observed Tycho twice, from 2022 June 20 to 2022 July 4 (observation ID 1001401) and from 2022 December 21 to 2022 December 25 (observation ID 02001601), for a total exposure time of ∼990 ks. We carried out the polarization analysis of the data with the publicly available software package *ixpeobssim* (Baldini et al. 2022), a simulation and analysis toolkit developed by the IXPE Collaboration that includes a tool for generating realistic Monte Carlo simulations of IXPE observations, as well as a full suite of post-processing applications able to select and process data to produce Stokes maps and spectra. We used version 11 of the IXPE response functions.

Our model-independent polarization analysis is based on the unbinned procedure described in Kislat et al. (2015). A weighted analysis could provide an increase in sensitivity (Peirson & Romani 2021; Di Marco et al. 2022); however, at the time of writing, a tool to perform it in a reproducible, model-independent way is not yet available. For this reason, we opted here for a simpler, but more consolidated, unweighted analysis procedure.

Before analyzing the data, we rejected the particle background by exploiting the possibility of distinguishing real events from non-X-ray particle events from the properties of the photoelectron tracks (Xie et al. 2021). We applied energy-independent cuts to the photoelectron track parameters recorded by the detector for each detected event and present in the *level 1* files, publicly distributed together with the *level 2* data. The photoelectron track parameters of interest for the rejection of the instrumental background (Xie et al. 2021, and Di Marco et al. 2023, submitted) are the size of the event-track region of interest (`NUM_PIX`), the fraction of the event energy in the track (PI major cluster/PI from all the clusters, `EVT_FRA`), and the number of border pixels in the track (`NUM_TRK`). The accepted events require that `NUM_PIX` < 250, `EVT_FRA` > 0.82, and `NUM_TRK` < 2. This cut rejects ∼30%

of the particle background while removing <1% of the source events. A logical mask describing the cuts is then applied to the level 2 data with the *ixpeobssim* selection tool *xpselect*.

We verified that the observation was not affected by increased particle background due to solar activity, and that the aspect of the spacecraft was stable during the observation, by checking the stability of the light curve of the background outside the SNR.

In the publicly released level 2 event list of the first observation (ObsID 01001401), a slight offset of the World Coordinate System (WCS) of about 10″–20″ was reported. We corrected this offset by employing a spatial correlation code previously applied for measuring the expansion of Cas A (Vink et al. 2022a). We registered the pointing solution of each detector unit to a 4–6 keV exposure-corrected Tycho image from Chandra (ObsID 10093), smoothed with $\sigma = 10.''4$. This energy band was chosen because the morphology is relatively independent of the energy response of the detectors. This operation resulted in a pointing solution with an accuracy of about 2″. The new absolute reference of the pixels (`CRVAL1`, `CRVAL2` in the file header) are, for the three DUs,

1. DU1 (R.A.; decl.): 6.32295; 64.14161,
2. DU2 (R.A.; decl.): 6.32267; 64.1412,
3. DU3 (R.A.; decl.): 6.32199; 64.14161.

No WCS correction was needed for the second observation (ObsID 02001601).

Due to an error in the reconstruction of the photons' absorption point in the GPD, the Stokes maps in sources with a large gradient of the brightness gradient—i.e., second derivative—can be contaminated on scales comparable to the IXPE angular resolution by spurious polarization patterns. However, we verified through estimates based on the Mueller matrix characterization of the IXPE response (Bucciantini et al. 2023) that this effect is negligible in all the Tycho regions of interest.

2.2. Data Analysis

In order to study polarized emission from Tycho, our analysis followed two approaches, including (1) a search for polarization on small-size scales, using a binned polarization map; and (2) a search for a large-scale polarization under the assumption of circular symmetry.

In both analysis approaches, we focus on the 3–6 keV band. We select this band in order to maximize our sensitivity to synchrotron emission where polarization is expected. In fact, in the full IXPE energy band of 2–8 keV, the Tycho spectrum includes very strong emission lines that are expected to be unpolarized. The 3–6 keV band is free of the Si, S, and Fe lines that have a high equivalent width with respect to the continuum. As demonstrated by prelaunch simulations using Chandra observations, this energy band also offers a better sensitivity for detecting polarization than the almost line-free (Ca K line at ∼4 keV is very weak) 4–6 keV continuum, despite the presence of the Ar-K line emission at ∼3.1 keV (Hwang & Gotthelf 1997).

2.2.1. Small-scale Search for Polarization

We first performed a spatial exploration of the polarization signal by producing binned maps of the Stokes parameters I, Q, U, by summing up the individual corresponding Stokes parameters of the events. The data from the three IXPE DUs were opportunely combined by passing the individual *level 2* event files, with the corrections described in the previous section applied, to the *xpbin* tool from *ixpeobbsim*. Using the *PMAPCUBE* algorithm of *xpbin*, we binned the maps with 1′ wide pixel sizes, corresponding to about twice the size of the IXPE angular resolution, in the 3–6 keV energy band. This procedure provides us with a polarization map showing the spatially resolved direction and degree of polarization.

2.2.2. Large-scale Search for Polarization

The large-scale search for polarization in the regions of interest was carried out with the *xpstokesalign* tool from *ixpeobssim*, which allows us to align the reconstructed Stokes parameters assuming a circular symmetry of the direction of the polarization with respect to a center. For each event, we recalculated the q_k and u_k Stokes parameters values by rotating their reference frame based on the sky position with respect to the geometrical center of Tycho—taken as R.A. = 6.340; decl. = 64.137 (Ruiz-Lapuente et al. 2004). The resulting new Stokes parameters q_k' and u_k' can be summed over the subset of region-selected events extracted with the *xpselect* tool and provide the total Stokes parameters from which we obtain the degree and angle of polarization. The angle convention is such that a direction of polarization with angle 0° indicates tangential polarization and 90° radial polarization. The aligned event lists were analyzed using *xpbin* with the *PCUBE* algorithm, which allows us to extract the Stokes parameters of the events collected in each region in the 3–6 keV band and calculate the polarization properties.

In Figure 1, we show a three-color image of Tycho with the regions considered in this work superimposed. We examine the regions identified by Eriksen et al. (2011) that correspond to structured synchrotron-emitting regions, i.e., the northeast knot (a), the west (b) the south stripes (c), the arch (d), and the synchrotron-emitting east knot (e). We also examine the region (f). The west region (f) is selected from the map of the significance of the measured degree of polarization that is distributed as χ^2_2 with two degrees of freedom and is shown in Figure 2. We produced this χ^2_2 significance map by the means described in detail in Appendix A of Vink et al. (2022b). The χ^2_2 significance map is smoothed with a Gaussian kernel with $\sigma = 10.''4$ and $10.''4$ pixel size, oversampling the IXPE angular resolution by a factor ∼2. We compute the probability that the value of the reduced χ^2 equals or exceeds a given value, z, which occurs as a random fluctuation from an unpolarized source as $\exp(-z/2)$—see Vink & Zhou (2018) and Appendix A of Vink et al. (2022b). In Figure 2, χ^2_2 values up to ∼35 can be seen in the west, which correspond to a chance probability of 2.5×10^{-8}. Finally, we consider the whole SNR as a circular region with 5′ radius, and the rim (g) as a 2′ wide annular region. In the former region, we aim to study the average polarization of the remnant, while the latter region contains the shell of shocked matter.

3. Results

A map of the direction and degree of polarization, binned on a 60″ pixel size that is about twice the IXPE angular resolution, is shown in Figure 3. The pixels with a significance lower than 1σ are masked. In the polarization map, we show the 4–6 keV contours based on Chandra observations, which serve as a

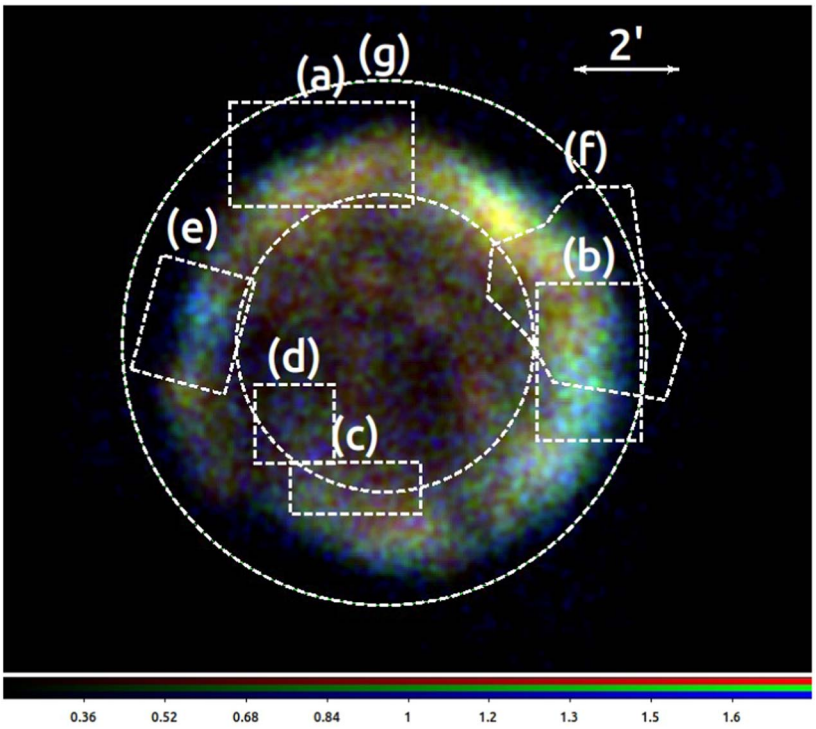

Figure 1. IXPE three-color image of Tycho combined from the three detectors based on the 2–3 keV (red), 3–4 keV (green), and 4–6 keV (blue) bands. Superimposed are the regions considered in this work: the northeast knot (a), the west stripes (b), the south stripes (c), and the arch (d) are the ones identified by Eriksen et al. (2011). The regions (e) and (f) are, respectively, the east knot and the west region where strong X-ray polarization is detected. Finally, the region (g) identifies the rim and the entire SNR.

point of reference for the location of the X-ray synchrotron emission.

This figure seems to suggest an overall tangential polarization pattern; however, with this choice of pixel size, only a few pixels, mostly on the western rim and highlighted with thicker cyan bars, have a significance above 2σ and none at 3σ.

In order to improve the statistics, rather than binning into larger pixels at the expense of potential depolarization due to mixing of signals from regions with different polarization properties, we exploit the rough spherical symmetry of Tycho and the fact that the remnant is known from radio observations to have a large-scale radially symmetric magnetic field. We thus compared the signals from the regions of interest shown in Figure 1 to those measured in the case of tangential polarization (that is, a radial magnetic field). As previously described, this allows us to sum the Stokes parameters over large regions and improve the statistics over the pixel-by-pixel search.

We express the significance of the measurement in number of sigmas, and we test the confidence level (CL) of the detection against the hypothesis of no polarization given the observed polarization and its uncertainty, computed using the cumulative distribution of χ^2 with two degrees of freedom. We consider 3σ as the statistical threshold to claim a probable detection.

We find that for the whole remnant, the rim region, the west region identified from the χ^2_2 map shown in Figure 2, and the west stripes, there are secure detections at 5.0σ, 6.0σ, 5.5σ, and 3.7σ, respectively, of the tangentially polarized signal. For the northeast and east knots, there is weak evidence for polarized emission with $\sigma > 2$. The south stripes and the arch do not show a significant polarization.

We correct the observed polarization for the dilution induced by the particle background, and the thermal plasma X-ray emission. The former is achieved by subtracting from the observation the Stokes parameters of a background present in the fields of extragalactic sources observed by IXPE. The latter is done by dividing the observed degree of polarization by the calculated fraction of the total emission associated with synchrotron radiation obtained from simulated IXPE maps based on Chandra data. This allows us to calculate the average intrinsic polarization PD_{Corr} of the synchrotron emission. The impact of the Galactic X-ray diffuse emission was evaluated through simulations and determined to be negligible. For the entire Tycho remnant, the degree of synchrotron polarization is $9\% \pm 2\%$. In the rim region, the polarization is $12\% \pm 2\%$. In the west—region (f)—we calculate the degree of polarization of the X-ray synchrotron emission to be $23\% \pm 4\%$. In the west stripes—region (b)— we derive a $14\% \pm 4\%$ degree of polarization. For the east, northeast, and south stripes, and the arch regions, we obtain synchrotron polarization upper limits at the 99% confidence level of $<32\%$, $<36\%$, $<29\%$, and $<35\%$, respectively. In all regions with a significant detection, the direction of polarization is compatible with a tangential direction of polarization.

The results are reported in Table 1 and shown in the form of a polar plot with confidence contours of the polarization parameters for each region in Figure 4: a direction of polarization consistent with 0° is in accordance with a tangential polarization.

4. Discussion

The IXPE observation of Tycho marks the first localized detection of X-ray polarization in an SNR, that is, the western

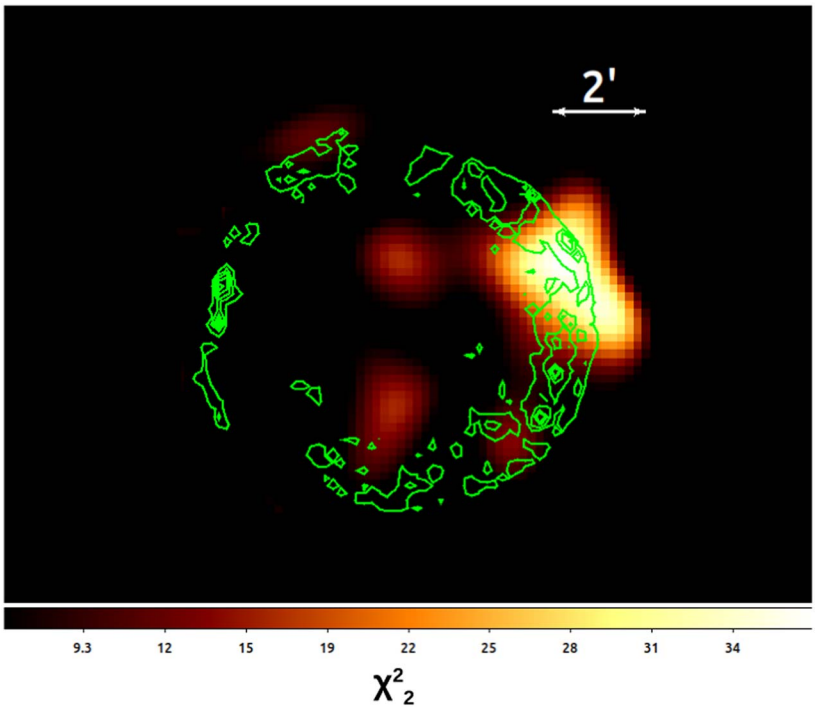

Figure 2. Map of χ^2_2—see Appendix A in Vink et al. (2022b)—values for the polarization signal in the 3–6 keV energy band smoothed with a Gaussian kernel. A χ^2_2 value of ∼35 corresponds to a probability of a random fluctuation from an unpolarized source equal to $\sim 10^{-8}$. Superimposed in green are the Chandra 4–6 keV contours.

region. IXPE observations of Cas A did significantly detect X-ray polarization, but only after summing over large annular regions (Vink et al. 2022b). Overall, we found a predominately radial magnetic field, as was also observed in the radio band. As this was also the conclusion of the IXPE observation of the core-collapse SNR Cas A (Vink et al. 2022b), the evidence that the processes responsible for the radial magnetic field observed in the radio band are already at work on the sub-parsec scales at which the X-rays are emitted ($\leqslant 10^{17}$ cm) is reinforced. However, in Tycho we found that the degree of X-ray polarization is higher than what was observed in Cas A, and even higher than its radio polarization (7%–8%). The degree of polarization of Tycho's rim, which includes the outer shock, is $12\% \pm 2\%$, while in the western region, the degree of polarization rises to values larger than 20%.

A number of effects in X-rays can lead to the observation of a degree of X-ray synchrotron radiation polarization higher than that observed in the radio band. First of all, X-ray synchrotron comes from teraelectronvolt-energy electrons, which, due to their very short lifetimes ($\ll$100 yr old), sample magnetic fields that are confined close to the sites where the electrons have been accelerated ($\leqslant 10^{17}$ cm, to be compared with the $\sim 10^{18}$ cm of the radio synchrotron emitted by approximately gigaelectronvolt electrons). Hence, because X-ray synchrotron-emitting regions occupy less volume than the radio synchrotron-emitting ones, depolarization due to different magnetic-field orientations along the line of sight is less likely in the X-ray band than in the radio band.

Moreover, the maximum degree of polarization depends on the photon index Γ of the synchrotron emission, with a steeper index resulting in a higher maximum polarization fraction Π (Ginzburg & Syrovatskii 1965)

$$\Pi_{\rm max} = \frac{\Gamma}{\Gamma + \frac{2}{3}}. \quad (1)$$

The X-ray synchrotron emission is associated with photon energies near the spectral cutoff; hence, its index is usually steeper than at longer wavelengths. Indeed, in the radio band young SNRs typically have $\Gamma \simeq 1.6$, while in the X-ray $\Gamma \simeq 3$, corresponding to $\mathrm{PD}_{\rm max} \simeq 82\%$ (Vink & Zhou 2018).

Finally, X-ray synchrotron emission does not sample the entire magnetic field, but may preferentially come from high magnetic-field regions, where the cutoff energies are pushed into the X-ray band (Vink & Zhou 2018). This effect further reduces the X-ray synchrotron emission volume, enhancing the degree of polarization—depending, however, on the spatial scale of the magnetic-field turbulence (see Bykov et al. 2009).

The IXPE observation of Cas A revealed a degree of polarization lower than, or at most equal to, the radio value. For Cas A, the authors invoked nearly isotropic magnetic-field turbulence or the mixing of a tangential magnetic field close to the shock with a radial one further downstream (Vink et al. 2022b). In the case of Tycho, a substantially larger polarization is measured than for Cas A. This either suggests a less turbulent magnetic field in Tycho than in Cas A, but it may also reflect a longer maximum scale of turbulence in Tycho than in Cas A. For the simulations in Bykov et al. (2020), the maximum wavelength scale for Tycho was $\sim 10^{18}$ cm, corresponding to 32″ at the distance of Tycho, comparable to the IXPE angular resolution. It was argued in Vink et al. (2022b) that for Cas A the maximum wavelength scale is substantially smaller than the IXPE resolution. For the turbulence of the upstream magnetic field, resonant magnetic-field turbulence generating Alfvén waves comparable in size to the gyroradius of the accelerated particles—i.e., $\lambda_{\rm max} \approx r_{\rm g} = E/eB = 6.5 \times 10^{15} (E_{\rm max}/10^{13}\ \mathrm{eV})\ (B/5\ \mu\mathrm{G})^{-1}$ cm—or nonresonant Bell instabilities (Bell 2004), are usually invoked. Equation (21) in Bell (2004) provides an estimate for the maximum size of the nonresonant mode, which

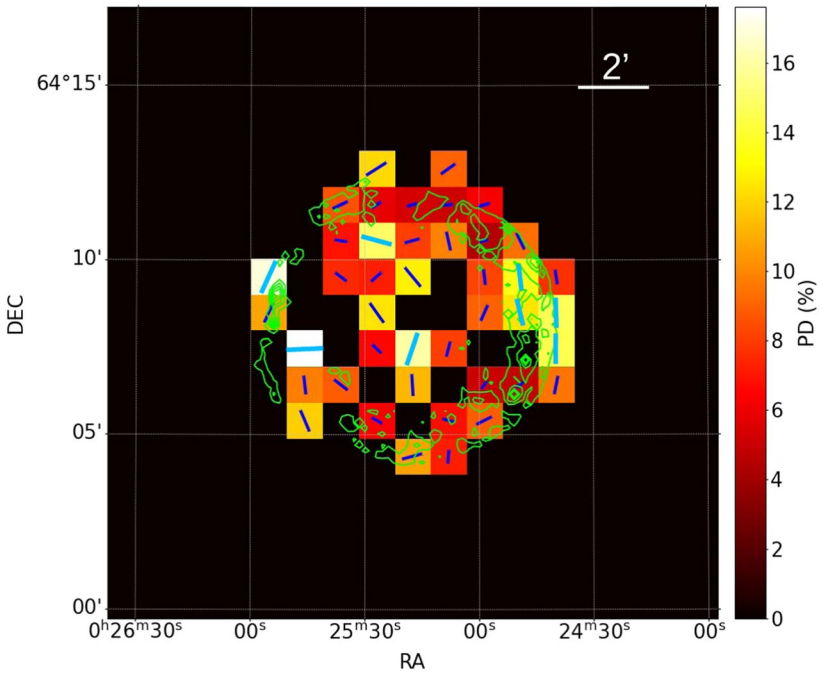

Figure 3. Polarization map in the 3–6 keV energy band with a 60″ pixel size. Only the pixels with significance higher than 1σ are shown. The blue bars represent the direction of the polarization (that is, the direction of the electric vector polarization angle) and their length is proportional to the degree of polarization. The thicker cyan bars mark the pixels with significance higher than 2σ. The orientation of the magnetic field is perpendicular to the direction of the polarization. Superimposed in green are the 4–6 keV Chandra contours.

scales as

$$\lambda_{\rm max} \approx 3 \times 10^{16} \left(\frac{V_{\rm s}}{4000\ {\rm km\ s^{-1}}}\right)^{-3} \left(\frac{n_0}{0.2\ {\rm cm^{-3}}}\right)^{-1} \times \left(\frac{B_0}{5\ \mu{\rm G}}\right) \left(\frac{E_{\rm max}}{2 \times 10^{13}\ {\rm eV}}\right) {\rm cm}, \quad (2)$$

with $V_{\rm s}$ the shock velocity, n_0 the pre-shock density, B_0 the pre-amplified magnetic-field strength, and $E_{\rm max}$ the cosmic-ray cutoff energy. Cas A has $E_{\rm max} = 5$ TeV (Ahnen et al. 2017), and a higher shock velocity (≈5500 km s^{-1}) and a higher density (2 cm^{-3}) with respect to Tycho (Williams et al. 2013, 2017; Archambault et al. 2017). For Cas A we estimate, based on this equation, $\lambda_{\rm max} \lesssim 4 \times 10^{15}$ cm, as its shock velocity and pre-shock densities are higher than Tycho's. Although for Tycho the maximum Bell's instability wavelength is longer than for Cas A, in both cases the wavelengths are substantially smaller than can be resolved by the IXPE resolution of ~10^{18} cm. So the higher polarization in Tycho compared to Cas A is not related to differences in turbulence modes created by Bell's instability. Moreover, the Bell instability operates on the unshocked plasma, and it is not clear what the implications are for the magnetic-field properties downstream of the shock. Clearly, the radial magnetic field reported here and for Cas A is perpendicular to what one expects after shock compression of a fully isotropic upstream magnetic field.

For the direction of the polarization, we find a clear indication of a tangential morphology, pointing toward the same radial magnetic-field orientation that is observed in the radio band for young SNRs. The origin of this radial magnetic field is still not well understood. West et al. (2017) proposed a selection effect due to the location where relativistic electrons pile up downstream of the shock. They argue that the spatial distribution of radio synchrotron-emitting electrons, accelerated at quasi-parallel shocks, can result in an apparent radial magnetic-field orientation, even if the overall field is actually disordered. Another possibility, discussed, e.g., by Inoue et al. (2013), is that the radial magnetic field can be established by a Rayleigh–Taylor or Richtmyer–Meshkov instability at, or near, the CD that produces filamentation. Within the anisotropic turbulence model of Bykov et al. (2020), when the magnetic field near the shock is predominantly radial, this pattern will produce polarization that is predominantly tangential to the SNR shock, with the degree of polarization of the order of a few tens percent, depending on the turbulence power spectrum index value.

Using the degree of polarization derived from this observation, we can put constraints on the magnetic-field amplification $\delta B/B$ using the model of Bandiera & Petruk (2016). Unlike Bykov et al. (2020), where the generation of magnetic turbulence is done with a full 3D numerical simulation, Bandiera & Petruk provide analytical formulae for the polarized fraction, generalizing the classical treatment of the synchrotron emission to the case of an ordered magnetic field plus a small-scale unresolved, isotropic, random Gaussian component, and also treat the case of shock compression of a fully random upstream field. They utilize a mean-field approach where the effect of magnetic turbulence is parametrized by the amount of total magnetic energy in the turbulent cascade. Their formalism, originally applied to the radio polarization of supernova shells, assumes a power-law energy distribution for the emitting electrons. This is not strictly correct for the X-rays, due to the presence of a cutoff. However, the dependence on the slope of the energy distribution is marginal (a minor increase in the degree of polarization is expected), over a very large range, so that at first order we can apply their model. For the rim, where we estimate a power-law index of the synchrotron emission of 2.82 ± 0.02, from the derived degree

Table 1
Results in the 3–6 keV Energy Band for Each Region of Interest

Region	Q/I (%)	U/I (%)	σ	CL (%)	PD (%)	PD_{Corr} (%)	P.A. (°)
All	3.5 ± 0.7	0.1 ± 0.7	5.0	>99.99	3.5 ± 0.7	9.1 ± 2.0	$1 \pm 6(7)$
Rim (g)	4.8 ± 0.8	-0.4 ± 0.8	6.0	>99.99	4.8 ± 0.8	11.9 ± 2.2	$-2 \pm 5(5)$
West, χ^2_2 (f)	9.7 ± 1.8	-2.6 ± 1.8	5.6	>99.99	10.0 ± 1.8	23.4 ± 4.2	$-7 \pm 5(5)$
West stripes (b)	7.1 ± 2.0	-1.7 ± 2.0	3.7	99.87	7.3 ± 2.0	13.9 ± 3.8	$-7 \pm 8(8)$
East (e)	7.3 ± 3.2	-3.5 ± 3.2	2.5	95.99	<16	<32	NC
Northeast (a)	5.0 ± 2.3	2.0 ± 2.3	2.4	94.07	<11	<36	NC
South stripes (c)	2.9 ± 3.6	0.0 ± 3.6	0.8	27.64	<12	<29	NC
Arch (d)	3.2 ± 4.3	0.5 ± 4.3	0.8	24.47	<14	<35	NC

Note. Q/I and U/I are the normalized observed Stokes parameters. The Stokes parameters are calculated under the hypothesis of a tangential polarization field (that would be $U/I = 0$ and $Q/I \neq 0$). The significance of the measurement expressed is σ, and CL the confidence level of the detection. The quoted uncertainties are 1σ, upper limits are at 99% confidence. PD and P.A. are the observed degree and angle of polarization, while PD_{Corr} is the degree of polarization of the synchrotron component only, calculated by correcting the observed degree of polarization by the instrumental background and the synchrotron fraction. In the regions where the observed polarization is below the MDP99 (minimum detectable polarization at 99% confidence), the direction of polarization is not constrained (NC).

of polarization of $12\% \pm 2\%$ the implied level of magnetic-field turbulence is $\delta B/B = 3.4 \pm 0.3$. In the west region, where the index is 2.90 ± 0.04 and the degree of polarization of $23\% \pm 4\%$, instead $\delta B/B = 2.2 \pm 0.4$. According to the model by Morlino & Caprioli (2012), for Tycho the magnetic-field amplification factor $\delta B/B$ can be ~20 downstream of the shock, with Landau damping at most halving it.

The observed polarization is thus inconsistent with the $\delta B/B \sim 10$–20 expected from acceleration models. This discrepancy could be explained by highly anisotropic magnetic-field turbulence. Alternatively, the X-ray synchrotron-emitting electrons may preferentially be situated in regions of low turbulence, or in regions where the magnetic-field orientation is preferentially radially oriented due to hydrodynamical instabilities.

5. Conclusions

We observed the Tycho SNR with IXPE, performing for the first time a spatially resolved measurement of its polarimetric properties in the 3–6 keV band. X-ray polarization measurements provided additional information on the geometry, turbulence, and amplification of the magnetic field at sub-parsec scales beyond what can be learned from the images alone. We performed both a pixel-by-pixel search for polarization and a large-scale search by assuming a circular symmetry of the polarization. We found in Tycho a predominantly radial magnetic field, as observed in the radio band. This result is in line with what IXPE found in the core-collapse SNR Cas A (Vink et al. 2022b), and further reinforces the evidence that the processes responsible for the radial magnetic field observed in the radio band are already at work on the scales at which the X-rays are emitted ($\leqslant 10^{17}$ cm). The degree of polarization of the Tycho rim, which includes the outer shock, is $12\% \pm 2\%$—higher than the 7%–8% observed in the radio band in the same region. In the western region, the degree of polarization rises to values larger than 20%. The implication is that the magnetic-field amplification factor in the shock region is 3.4 ± 0.3, far from the factor 10–20 expected from particle acceleration models. This suggests a highly anisotropic magnetic field, as proposed by Bykov et al. (2020), or that the X-ray synchrotron-emitting electrons may preferentially select regions of either low turbulence, or where the magnetic-field orientation is preferentially radially oriented due to hydrodynamical instabilities.

From the comparison with the IXPE observation of Cas A, we find a larger degree of X-ray polarization in Tycho. This could be evidence of a more ordered magnetic field, but it could also be a result of a longer maximum turbulence scale in Tycho than in Cas A. However, this difference in turbulence scale cannot be attributed to Bell's instability. Future, dedicated simulations based on these results will allow one to improve the existing models of magnetic-field turbulence and particle acceleration at the shocks of young SNRs.

IXPE is a joint US and Italian mission. The US contribution is supported by the National Aeronautics and Space Administration (NASA) and led and managed by its Marshall Space Flight Center (MSFC), with industry partner Ball Aerospace (contract NNM15AA18C). The Italian contribution is supported by the Italian Space Agency (Agenzia Spaziale Italiana, ASI) through contract ASI-OHBI-2017-12-I.0, agreements ASI-INAF-2017-12-H0 and ASI-INFN-2017.13-H0, and its Space Science Data Center (SSDC) with agreements ASI-INAF-2022-14-HH.0 and ASI-INFN 2021-43-HH.0, and by the Istituto Nazionale di Astrofisica (INAF) and the Istituto Nazionale di Fisica Nucleare (INFN) in Italy. This research used data products provided by the IXPE Team (MSFC, SSDC, INAF, and INFN) and distributed with additional software tools by the High-Energy Astrophysics Science Archive Research Center (HEASARC), at NASA Goddard Space Flight Center (GSFC).

J. Vink & D.Prokhorov are supported by funding from the European Union's Horizon 2020 research and innovation program under grant agreement No. 101004131 (SHARP). P.S. acknowledges support from NASA contract NAS8-03060. P.Z. acknowledges the support from NWO Veni Fellowship grant No. 639.041.647 and NSFC grant No. 12273010 C.-Y.N. and Y.J.Y. are supported by a GRF grant of the Hong Kong Government under HKU 17305419. We thank the anonymous reviewer for their useful comments and suggestions.

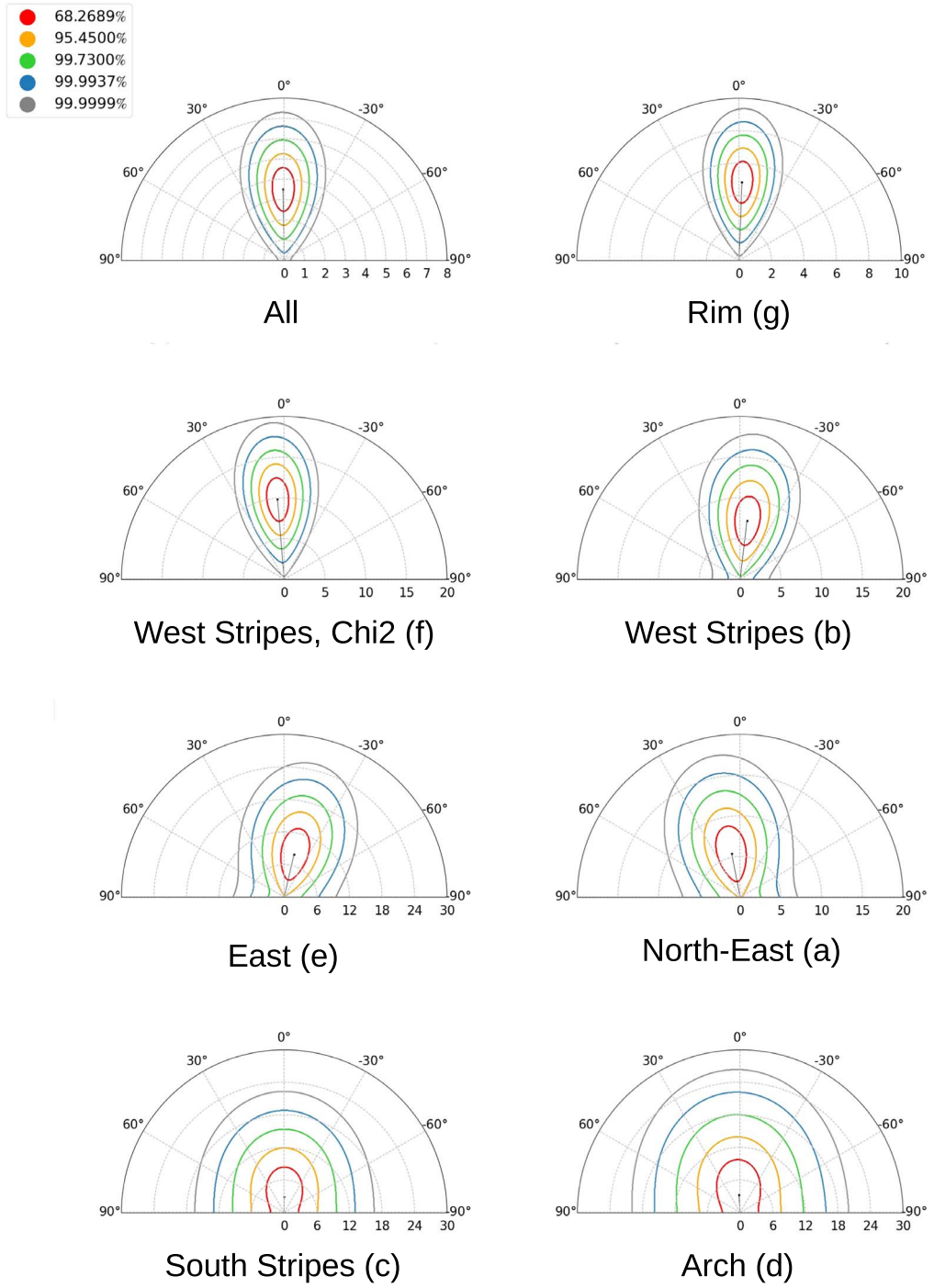

Figure 4. Polar plots for the Tycho regions of interest considered in this work. Each diagram depicts the measured degree of polarization and direction with respect to a circular symmetry and the geometrical center of the remnant, as confidence contours for the regions listed in Table 1. The confidence levels given are color coded in the legend. The radial coordinate indicates the degree of polarization in percent. Values more consistent with a direction of polarization of 0° correspond to an overall tangentially oriented polarization averaged over the region.

Facilities: IXPE, Chandra.

Software: ixpeobssim (Baldini et al. 2022), CIAO (Fruscione et al. 2006), XSPEC (Arnaud 1996).

Appendix A
Assessment of the Background Contribution Across Tycho

The region outside the SNR is too small and close to the detector edges for use to obtain a statistically significant and reliable background to subtract from the data because of detector-border effects due to incomplete photoelectron track collection at the edges of the sensitive area.

We estimated the combined particle and extragalactic background contribution by accumulating ∼2 Ms worth of publicly available IXPE observations of high Galactic latitude blazars and other extragalactic point sources. From the observations listed in Table 2 marked as background observations, we extracted annular regions centered on the point sources with an inner radius of 2′ and an outer radius of 5′. We

Table 2
Observations Used in This Work for Data Analysis and Background Extraction

Mission	ObsID	Start Date (YYYY-MM-DD)	Effective Exposure (ks)	Notes
IXPE	01001401	202 2-6-20	771	Tycho observation
IXPE	02001601	2022-12-21	216	Tycho observation
Chandra	10093	2009-4-13	118.3	Tycho observation, WCS correction
Chandra	10095	2009-4-23	173.4	Tycho observation, spectra extraction
IXPE	1003701	2022-5-4	96.7	Mrk421, background
IXPE	1003801	2022-6-4	96.0	Mrk421, background
IXPE	1004501	2022-3-8	100.4	Mrk501, background
IXPE	1004701	2022-7-9	97.8	Mrk501, background
IXPE	1006301	2022-5-6	390.9	BL Lac, background
IXPE	1006301	2022-5-6	116.9	BL Lac, background
IXPE	1003501	2022-7-12	771.8	Circinus, background
IXPE	1005701	2022-6-12	264.2	3C279, background

applied the previously described rejection algorithm to these background observations to ensure consistency with the Tycho observation, and then summed the Stokes parameters of each background region. This allows for each source to have a uniform background extraction region that is not contaminated by either border effects, or polarization from the source. We found that the background is consistent with no polarization (i.e., the normalized Stokes parameters are compatible with having a value of 0 within the uncertainty) with an MDP99 of 3.7% in the 3–6 keV. We recall that the MDP99 (see Weisskopf et al. 2010) is defined as the degree of polarization corresponding to the amplitude of modulation that has only a 1% probability of being detected by chance. The normalized and scaled Stokes parameters of the background for each region of interest are reported in Table 3 and are compatible with 0. Because the aforementioned background is compatible with null polarization, its Stokes parameters—after appropriately scaling them for the region areas and exposure time—can be safely subtracted from the Tycho observation and the uncertainties on the Stokes parameters linearly propagated to the polarimetric observables. The rate of the background in the 3–6 keV band is 2.0×10^{-2} counts s^{-1} cm^{-2} keV^{-1}, to be compared with the Tycho rate of 9.1×10^{-2} counts s^{-1} cm^{-2} keV^{-1}.

We also evaluated the contribution of the Galactic X-ray diffuse emission (GXDE) from Chandra observations of regions close to Tycho. The dilution of the degree of polarization due to the Galactic background sources is evaluated through the complement to unity, so that we express in the following the dilution D as

$$D = 1 - \frac{P_{\rm dil}}{P_0} = 1 - \frac{1}{1 + \frac{R_B}{R_S}}, \quad \text{(A1)}$$

where $P_{\rm dil}$ and P_0 are the degrees of diluted and intrinsic polarization, respectively, and R_B and R_S are the source and background rates. The lower the value of this dilution, the smaller the impact of the background on the observed signal. To estimate the IXPE counting rate of the GXDE we extracted from a Chandra observation (ObsID 10095) the blank sky-subtracted and point-source-removed spectrum from regions outside of Tycho and we fitted the spectrum of the background region with the model from Ebisawa et al. (2005). To obtain the IXPE counting rate, we used this spectral fit as input to *ixpeobssim* with a uniform disk morphology the same size as the region of interest and no polarization. We find that for the whole remnant, the counting rate of the GXDE is 2.5×10^{-3} counts s^{-1} cm^{-2} keV^{-1}, so that the degree of polarization in the 3–6 keV band is diluted by the GXDE by a relative factor of 2.7%. Because this dilution is much smaller than the statistical

Table 3
Background Stokes Parameters and Synchrotron Fraction Calculated for Each Region of Interest in the 3–6 keV Energy Band

Region	Q/I (%)	U/I (%)	Synchrotron Fraction
All	0.05 ± 0.06	-0.02 ± 0.06	0.51
Rim (g)	0.03 ± 0.04	-0.01 ± 0.04	0.53
West, χ^2_2 (f)	0.006 ± 0.007	-0.003 ± 0.007	0.52
West stripes (b)	0.004 ± 0.004	-0.002 ± 0.004	0.61
East (e)	0.003 ± 0.003	-0.001 ± 0.003	0.69
Northeast (a)	0.005 ± 0.005	-0.002 ± 0.005	0.41
South stripes (c)	0.002 ± 0.002	-0.001 ± 0.002	0.53
Arch (d)	0.001 ± 0.002	-0.001 ± 0.002	0.55

Note. The normalized Stokes parameters of the background are scaled for the region surface and exposure time.

uncertainty of the measurements, we consider it to be negligible.

Appendix B
Assessment of Synchrotron Contribution across Tycho

In the IXPE energy band of 2–8 keV, the emission from the Tycho SNR consists of both thermal components—such as bremsstrahlung, line emission, free-bound, and two-photon emission—and nonthermal synchrotron radiation (Hwang et al. 2002). In order to estimate the contribution of the synchrotron radiation to each IXPE region of interest as a function of energy, we modeled the emission from Tycho by dividing a single 173.37 ks long Chandra observation (ObsID 10095) into 624 20×20 arcsec^2 boxes as shown in Figure 5. From each box, we extracted the spectrum and fitted it with the XSPEC package version 12.12 (Arnaud 1996). We used two thermal components for ejecta and a nonthermal synchrotron component as *tbabs ∗ (vpshock+vpshock+powerlaw)*. The two thermal *vpshock* components correspond to the N–O–Ne–Mg–Si–S–Ar–Ca, and Fe–Ni-rich plasmas, respectively. In the former, the Fe abundance is set to zero, in the latter is a free parameter, while the other elements are set to solar abundance (Hwang & Gotthelf 1997). Normalizations, temperatures, photon index, and $N_{\rm H}$ are obtained from the fit to the Chandra data. Because they are based on an automated procedure, we do not claim that these are the best possible models for the emission of Tycho; however, they work reasonably well for the purpose of this work, which is to obtain an estimate of the synchrotron fraction and not to perform deep spectroscopy. In Figure 6 we show a histogram of the distribution of the fit of the power-law spectral index Γ, the temperature of the Fe–Ni-rich plasma kT_1, the temperature of the N–O–Ne–Mg–Si–S–Ar–Ca-rich plasma kT_2, and the column density $N_{\rm H}$. In the majority of the boxes, the fit provided reasonable parameter values, with $\Gamma \sim 3.1$, $kT_1 \sim 6.7$, $kT_2 \sim 2.2$, and $N_{\rm H} \sim 0.56$ (Hwang & Gotthelf 1997; Hwang et al. 2002; Decourchelle 2017). Having obtained for each box the best-fit model of the spectrum, we folded them through the IXPE spatial and spectral response functions using the *xpobssim* Monte Carlo simulation tool from *ixpeobssim* as a region of interest with 2×624 sources. Each of the 624 elements is treated in the simulation as two independent extended sources corresponding to the thermal and nonthermal spectral components. In *ixpeobssim*, these sources are defined by an energy spectrum from the output of XSPEC for the single spectral component of interest and by an image from Chandra to trace the local morphology of the emission. A Chandra image of the box in the 2–3 and 4–6 keV bands is attached to the thermal and nonthermal components, respectively, to trace the local morphology of the emission. We simulated two 5 Ms long IXPE observations (sufficiently long to smooth out any statistical fluctuations): one considering the total emission and one with the nonthermal emission only. Since we are interested only in the relative emission from the nonthermal and total components, we assume the source model to be unpolarized and we do not include the instrumental background in the simulation. From the ratio of the simulated nonthermal and total intensities, we obtain for each region of interest from Table 1—selected from the simulated data with *xpselect* in the same way as done for the observation—an estimate of the fraction of the source emission that is due to synchrotron radiation only. We divide in each region of interest the background subtracted polarization by the estimated synchrotron fraction to obtain the corrected degree of polarization $\rm PD_{corr}$. The synchrotron fraction map in the 3–6 keV energy band, binned on a pixel size of 30″ is shown in Figure 7, while in Table 3 we report the calculated synchrotron fraction for each region of interest.

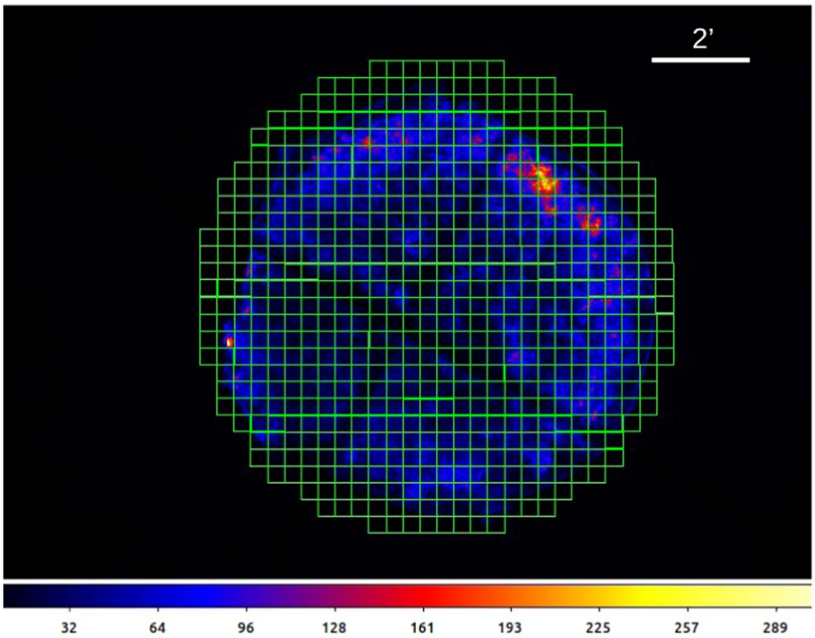

Figure 5. Grid made of the 624 20×20 arcsec^2 boxes for spectra and image extraction used in the synchrotron fraction map simulation, superimposed on the Chandra observation of Tycho (ObsID 10095).

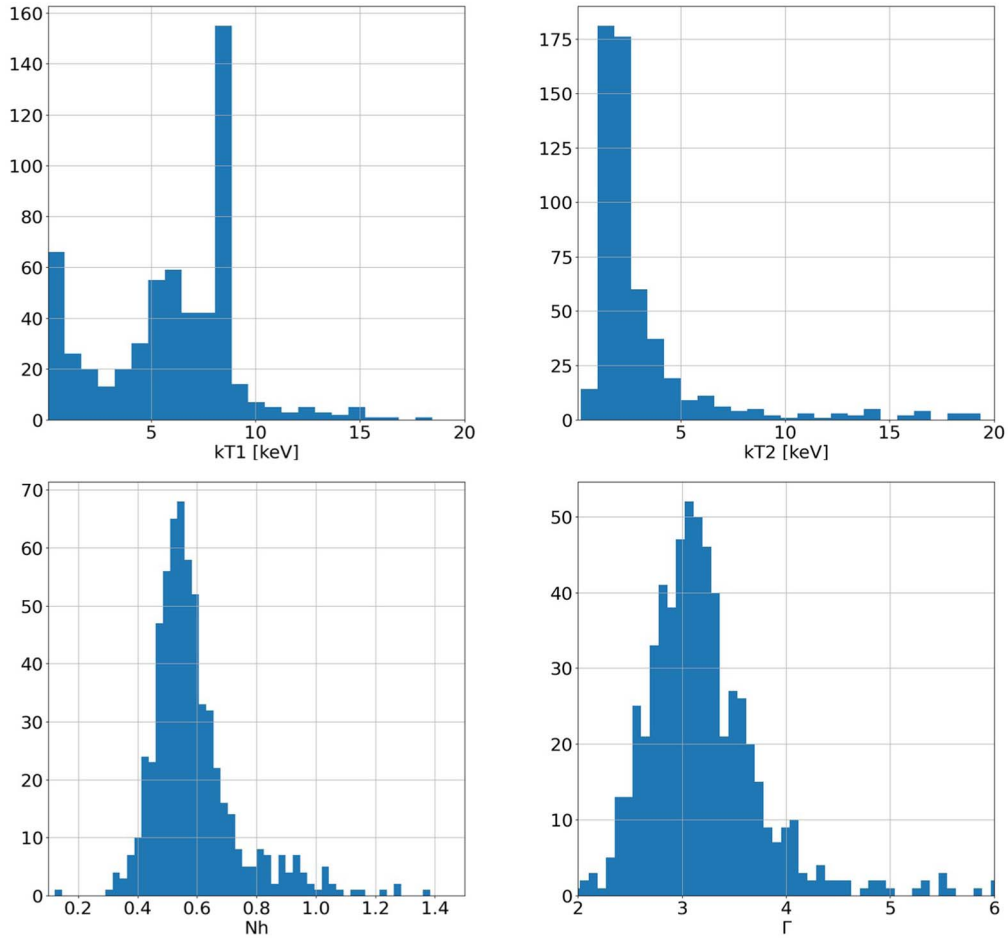

Figure 6. Histogram of the distribution of the best fit of the spectral parameters kT_1, kT_2, $N_{\rm H}$, and Γ in the 624 extraction boxes.

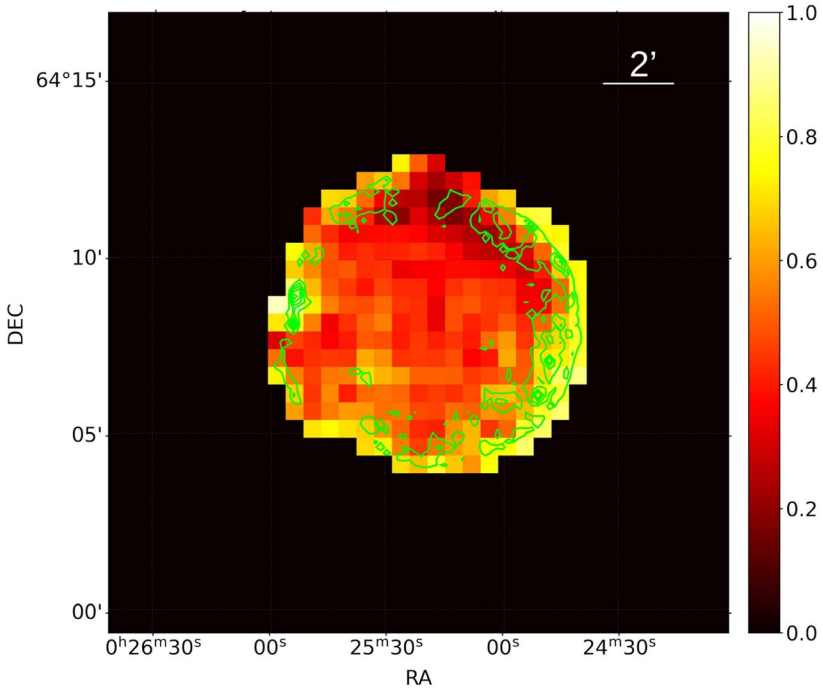

Figure 7. Simulated Tycho synchrotron fraction map in the 3–6 keV binned on a pixel size of 30″ with the Chandra contours of the 4–6 keV emission overlaid in green.

ORCID iDs

Riccardo Ferrazzoli https://orcid.org/0000-0003-1074-8605
Patrick Slane https://orcid.org/0000-0002-6986-6756
Ping Zhou https://orcid.org/0000-0002-5683-822X
Jacco Vink https://orcid.org/0000-0002-4708-4219
Niccolò Bucciantini https://orcid.org/0000-0002-8848-1392
Enrico Costa https://orcid.org/0000-0003-4925-8523
Niccolò Di Lalla https://orcid.org/0000-0002-7574-1298
Alessandro Di Marco https://orcid.org/0000-0003-0331-3259
Paolo Soffitta https://orcid.org/0000-0002-7781-4104
Martin C. Weisskopf https://orcid.org/0000-0002-5270-4240
Luca Baldini https://orcid.org/0000-0002-9785-7726
Jeremy Heyl https://orcid.org/0000-0001-9739-367X
Philip E. Kaaret https://orcid.org/0000-0002-3638-0637
Frédéric Marin https://orcid.org/0000-0003-4952-0835
Tsunefumi Mizuno https://orcid.org/0000-0001-7263-0296
C.-Y. Ng https://orcid.org/0000-0002-5847-2612
Melissa Pesce-Rollins https://orcid.org/0000-0003-1790-8018
Carmelo Sgrò https://orcid.org/0000-0001-5676-6214
Douglas A. Swartz https://orcid.org/0000-0002-2954-4461
Toru Tamagawa https://orcid.org/0000-0002-8801-6263
Yi-Jung Yang https://orcid.org/0000-0001-9108-573X
Iván Agudo https://orcid.org/0000-0002-3777-6182
Lucio A. Antonelli https://orcid.org/0000-0002-5037-9034
Matteo Bachetti https://orcid.org/0000-0002-4576-9337
Wayne H. Baumgartner https://orcid.org/0000-0002-5106-0463
Ronaldo Bellazzini https://orcid.org/0000-0002-2469-7063
Stefano Bianchi https://orcid.org/0000-0002-4622-4240
Stephen D. Bongiorno https://orcid.org/0000-0002-0901-2097
Raffaella Bonino https://orcid.org/0000-0002-4264-1215
Alessandro Brez https://orcid.org/0000-0002-9460-1821
Fiamma Capitanio https://orcid.org/0000-0002-6384-3027
Simone Castellano https://orcid.org/0000-0003-1111-4292
Elisabetta Cavazzuti https://orcid.org/0000-0001-7150-9638
Chien-Ting Chen https://orcid.org/0000-0002-4945-5079
Stefano Ciprini https://orcid.org/0000-0002-0712-2479
Alessandra De Rosa https://orcid.org/0000-0001-5668-6863
Ettore Del Monte https://orcid.org/0000-0002-3013-6334
Laura Di Gesu https://orcid.org/0000-0002-5614-5028
Immacolata Donnarumma https://orcid.org/0000-0002-4700-4549
Victor Doroshenko https://orcid.org/0000-0001-8162-1105
Michal Dovčiak https://orcid.org/0000-0003-0079-1239
Steven R. Ehlert https://orcid.org/0000-0003-4420-2838
Teruaki Enoto https://orcid.org/0000-0003-1244-3100
Yuri Evangelista https://orcid.org/0000-0001-6096-6710
Sergio Fabiani https://orcid.org/0000-0003-1533-0283
Javier A. Garcia https://orcid.org/0000-0003-3828-2448
Shuichi Gunji https://orcid.org/0000-0002-5881-2445
Wataru Iwakiri https://orcid.org/0000-0002-0207-9010
Svetlana G. Jorstad https://orcid.org/0000-0001-6158-1708
Fabian Kislat https://orcid.org/0000-0001-7477-0380
Vladimir Karas https://orcid.org/0000-0002-5760-0459
Jeffery J. Kolodziejczak https://orcid.org/0000-0002-0110-6136
Henric Krawczynski https://orcid.org/0000-0002-1084-6507
Fabio La Monaca https://orcid.org/0000-0001-8916-4156
Luca Latronico https://orcid.org/0000-0002-0984-1856
Ioannis Liodakis https://orcid.org/0000-0001-9200-4006
Simone Maldera https://orcid.org/0000-0002-0698-4421
Alberto Manfreda https://orcid.org/0000-0002-0998-4953
Andrea Marinucci https://orcid.org/0000-0002-2055-4946
Alan P. Marscher https://orcid.org/0000-0001-7396-3332
Herman L. Marshall https://orcid.org/0000-0002-6492-1293
Giorgio Matt https://orcid.org/0000-0002-2152-0916
Fabio Muleri https://orcid.org/0000-0003-3331-3794
Michela Negro https://orcid.org/0000-0002-6548-5622
Stephen L. O'Dell https://orcid.org/0000-0002-1868-8056
Nicola Omodei https://orcid.org/0000-0002-5448-7577
Chiara Oppedisano https://orcid.org/0000-0001-6194-4601
Alessandro Papitto https://orcid.org/0000-0001-6289-7413
George G. Pavlov https://orcid.org/0000-0002-7481-5259
Abel L. Peirson https://orcid.org/0000-0001-6292-1911
Matteo Perri https://orcid.org/0000-0003-3613-4409
Pierre-Olivier Petrucci https://orcid.org/0000-0001-6061-3480
Maura Pilia https://orcid.org/0000-0001-7397-8091
Andrea Possenti https://orcid.org/0000-0001-5902-3731
Juri Poutanen https://orcid.org/0000-0002-0983-0049
Simonetta Puccetti https://orcid.org/0000-0002-2734-7835
Brian D. Ramsey https://orcid.org/0000-0003-1548-1524
John Rankin https://orcid.org/0000-0002-9774-0560
Ajay Ratheesh https://orcid.org/0000-0003-0411-4243
Oliver Roberts https://orcid.org/0000-0002-7150-9061
Roger W. Romani https://orcid.org/0000-0001-6711-3286
Gloria Spandre https://orcid.org/0000-0003-0802-3453
Fabrizio Tavecchio https://orcid.org/0000-0003-0256-0995
Roberto Taverna https://orcid.org/0000-0002-1768-618X
Allyn F. Tennant https://orcid.org/0000-0002-9443-6774
Nicholas E. Thomas https://orcid.org/0000-0003-0411-4606
Francesco Tombesi https://orcid.org/0000-0002-6562-8654
Alessio Trois https://orcid.org/0000-0002-3180-6002
Sergey S. Tsygankov https://orcid.org/0000-0002-9679-0793
Roberto Turolla https://orcid.org/0000-0003-3977-8760
Kinwah Wu https://orcid.org/0000-0002-7568-8765
Fei Xie https://orcid.org/0000-0002-0105-5826
Silvia Zane https://orcid.org/0000-0001-5326-880X

References

Ahnen, M. L., Ansoldi, S., Antonelli, L. A., et al. 2017, MNRAS, 472, 2956
Amato, E. 2014, IJMPD, 23, 1430013
Archambault, S., Archer, A., Benbow, W., et al. 2017, ApJ, 836, 23
Arnaud, K. A. 1996, in ASP Conf. Ser. 101, Astronomical Data Analysis Software and Systems V, ed. G. H. Jacoby & J. Barnes (San Francisco, CA: ASP), 17
Baldini, L., Bucciantini, N., Lalla, N. D., et al. 2022, SoftX, 19, 101194
Bandiera, R., & Petruk, O. 2016, MNRAS, 459, 178
Baring, M. G. 2017, in IAU Symp. 331, Supernova 1987A: 30 Years Later—Cosmic Rays and Nuclei from Supernovae and Their Aftermaths, ed. A. Marcowith (Cambridge: Cambridge Univ. Press), 242
Bell, A. R. 2004, MNRAS, 353, 550
Bykov, A. M., Ellison, D. C., Osipov, S. M., Pavlov, G. G., & Uvarov, Y. A. 2011, ApJL, 735, L40
Bucciantini, N., Di Lalla, N., Romani, R., et al. 2023, arXiv:2302.00346

Bykov, A. M., Uvarov, Y. A., Bloemen, J. B. G. M., den Herder, J. W., & Kaastra, J. S. 2009, MNRAS, 399, 1119
Bykov, A. M., Uvarov, Y. A., Slane, P., & Ellison, D. C. 2020, ApJ, 899, 142
Decourchelle, A. 2017, in Handbook of Supernovae, ed. A. W. Alsabti & P. Murdin (Cham: Springer), 117
Di Marco, A., Costa, E., Muleri, F., et al. 2022, AJ, 163, 170
Di Marco, A., Soffitta, P., Costa, E., et al. 2023, AJ, submitted
Dickel, J. R., van Breugel, W. J. M., & Strom, R. G. 1991, AJ, 101, 2151
Dubner, G., & Giacani, E. 2015, A&ARv, 23, 3
Duin, R. M., & Strom, R. G. 1975, A&A, 39, 33
Ebisawa, K., Tsujimoto, M., Paizis, A., et al. 2005, ApJ, 635, 214
Eriksen, K. A., Hughes, J. P., Badenes, C., et al. 2011, ApJL, 728 L28
Ferrazzoli, R., Muleri, F., Lefevre, C., et al. 2020, JATIS, 6, 048002
Fruscione, A., McDowell, J. C., Allen, G. E., et al. 2006, Proc. SPIE, 6270, 62701V
Ginzburg, V. L., & Syrovatskii, S. I. 1964, The Origin of Cosmic Rays (New York: Macmillan)
Ginzburg, V. L., & Syrovatskii, S. I. 1965, ARA&A, 3, 297
Green, D. A., & Stephenson, F. R. 2003, in Supernovae and Gamma-Ray Bursters, ed. K. Weiler, Vol. 598 (Berlin: Springer), 7
Hwang, U., Decourchelle, A., Holt, S. S., & Petre, R. 2002, ApJ, 581, 1101
Hwang, U., & Gotthelf, E. V. 1997, ApJ, 475, 665
Inoue, T., Shimoda, J., Ohira, Y., & Yamazaki, R. 2013, ApJL, 772, L20
Jun, B. I., & Norman, M. L. 1996, ApJ, 472, 245
Kislat, F., Clark, B., Beilicke, M., & Krawczynski, H. 2015, APh, 68, 45
Kundu, M. R., & Velusamy, T. 1971, ApJ, 163, 231
Malkov, M. A., & Drury, L. O. 2001, RPPh, 64, 429
Matsuda, M., Tanaka, T., Uchida, H., Amano, Y., & Tsuru, T. G. 2020, PASJ, 72, 85
Morlino, G., & Caprioli, D. 2012, A&A, 538, A81
Okuno, T., Tanaka, T., Uchida, H., et al. 2020, ApJ, 894, 50
Peirson, A. L., & Romani, R. W. 2021, ApJ, 920, 40
Rankin, J., Muleri, F., Tennant, A. F., et al. 2022, AJ, 163, 39
Reynolds, S. P., Williams, B. J., Borkowski, K. J., & Long, K. S. 2021, ApJ, 917, 55
Reynoso, E. M., Moffett, D. A., Goss, W. M., et al. 1997, ApJ, 491, 816
Richtmyer, R. D. 1960, Commun. Pure Appl. Math., 13, 297
Ruiz-Lapuente, P., Comeron, F., Méndez, J., et al. 2004, Natur, 431, 1069
Soffitta, P., Baldini, L., Bellazzini, R., et al. 2021, AJ, 162, 208
Strom, R. G., & Duin, R. M. 1973, A&A, 25, 351
Vink, J., Patnaude, D. J., & Castro, D. 2022a, ApJ, 929, 57
Vink, J., Prokhorov, D., Ferrazzoli, R., et al. 2022b, ApJ, 938, 40
Vink, J., & Zhou, P. 2018, Galax, 6, 46
Weisskopf, M. C., Elsner, R. F., & O'Dell, S. L. 2010, Proc. SPIE, 7732, 77320E
Weisskopf, M. C., Soffitta, P., Baldini, L., et al. 2022, JATIS, 8, 026002
West, J. L., Jaffe, T., Ferrand, G., Safi-Harb, S., & Gaensler, B. M. 2017, ApJL, 849, L22
Williams, B. J., Borkowski, K. J., Ghavamian, P., et al. 2013, ApJ, 770, 129
Williams, B. J., Coyle, N. M., Yamaguchi, H., et al. 2017, ApJ, 842, 28
Williams, B. J., Katsuda, S., Cumbee, R., et al. 2020, ApJL, 898, L51
Xie, F., Ferrazzoli, R., Soffitta, P., et al. 2021, APh, 128, 102566
Zirakashvili, V. N., & Ptuskin, V. S. 2008, ApJ, 678, 939